

Chiral dynamics in the low-temperature phase of QCD

Bastian B. Brandt

Institut für theoretische Physik, Universität Regensburg, D-93040 Regensburg

Anthony Francis, Harvey B. Meyer, Daniel Robaina

*PRISMA Cluster of Excellence, Institut für Kernphysik and Helmholtz Institut Mainz,
Johannes Gutenberg-Universität Mainz, D-55099 Mainz, Germany*

(Dated: October 10, 2018)

We investigate the low-temperature phase of QCD and the crossover region with two light flavors of quarks. The chiral expansion around the point $(T, m = 0)$ in the temperature vs. quark-mass plane indicates that a sharp real-time excitation exists with the quantum numbers of the pion. An exact sum rule is derived for the thermal modification of the spectral function associated with the axial charge density; the (dominant) pion pole contribution obeys the sum rule. We determine the two parameters of the pion dispersion relation using lattice QCD simulations and test the applicability of the chiral expansion. The time-dependent correlators are also analyzed using the Maximum Entropy Method, yielding consistent results. Finally, we test the predictions of the chiral expansion around the point $(T = 0, m = 0)$ for the temperature dependence of static observables.

I. INTRODUCTION & MAIN RESULTS

Quark matter at temperatures say $T \gtrsim 30$ MeV is both of intrinsic interest as a strongly interacting, quantum relativistic system, and of relevance in the first few microseconds of the early universe; see for instance [1], chapter D. It is studied intensively in heavy-ion collisions. For small values of the average up and down quark mass m , the system undergoes a transition from a low-temperature phase where the longest static correlation length, m_π^{-1} , scales as $1/\sqrt{m}$ to a high-temperature phase where the correlation length is largely insensitive to m .

One picture of the low-temperature phase that has had significant phenomenological success is the hadron resonance gas (HRG) model. It assumes that the thermodynamic properties of the system, including the conserved charge fluctuations, are given by the sum of the partial contributions of non-interacting hadron species. The sum extends over all resonances of mass up to about 2.5 GeV, since for most of them the width is not large compared to the temperature. The model gives an economic description of particle yields in heavy-ion collisions (see the recent [2], [3] and references therein) and gives a good estimate of the pressure and charge fluctuations determined in lattice calculations [4–6]. On the other hand, relatively little is known with certainty about the spectral functions of local operators (say, the conserved vector current, the axial current or the energy-momentum tensor) at finite temperature, which encode the real-time excitations of the system [7]. The success of the HRG model for static quantities does not imply that the real-time excitations of the system are in any sense similar to the ordinary QCD resonances observed at $T = 0$.

A good starting point to investigate the excitations of the thermal medium is to study what becomes of the pion [8, 9]. At sufficiently low temperatures $T \ll T_c$, correlation func-

tions can be computed using chiral perturbation theory. The result is that a well-defined pion quasiparticle persists, with small modifications to the real part of the pole, and a parametrically small imaginary part [10–12]. It is not clear how far up in temperature this treatment can be justified, since the partition function is certainly no longer dominated by the pions for $T \gtrsim 100$ MeV. However, the pion is special in that the Goldstone theorem guarantees the presence of a divergent static correlation length when $m \rightarrow 0$ for all temperatures in the chirally broken phase [13]. If we consider the temperature vs. quark-mass plane (T, m) , this observation suggests an expansion in the quark mass around the point $(T, 0)$. In this case, one gives up on relating the chiral condensate $\langle \bar{\psi}\psi \rangle$ and the screening pion amplitude f_π to their $T = 0$ counterparts, however the range of applicability is significantly extended; see Fig. 1. This is the approach adopted by Son and Stephanov [14, 15]. The result of their analysis is that a pion quasiparticle persists, with a parametrically small imaginary part compared to the real part of the pole position. The real part of its dispersion relation is, however, no longer the relation implied by Lorentz invariance, but rather

$$\omega_{\mathbf{k}}^2 = u^2(m_\pi^2 + \mathbf{k}^2) + \dots \quad (1)$$

Here m_π is the inverse static correlation length in the pseudoscalar channel, and u , the ‘pion velocity’, is an a priori unknown function of temperature which can however be related to static quantities [15]. Determining $u(T)$ using lattice QCD for a few temperatures below T_c is one of the main goals of this paper. We first rederive Eq. (1), present an improved estimator for $u(T)$, and show that the spectral function ρ_A of the axial charge density obeys the following exact sum rule for all temperatures, quark masses and spatial momenta,

$$\int_{-\infty}^{\infty} d\omega \, \omega \, \rho_A(\omega, \mathbf{k}) \Big|_0^T = -m \langle \bar{\psi}\psi \rangle \Big|_0^T. \quad (2)$$

The respective pion pole contributions (which dominate) at zero and at finite temperature satisfy the sum rule.

We will be working in QCD with two flavors of ($O(a)$ improved Wilson) quarks with renormalized masses $8\text{MeV} \leq \bar{m}^{\overline{\text{MS}}} \leq 15\text{MeV}$. In this range of quark masses, the transition from the low-temperature to the high-temperature phase is a crossover, as it is at physical quark masses. At vanishing m , there must be a sharp phase transition, however its nature is not known with certainty¹. The crossover temperature, defined conventionally by some observable, depends quite strongly on the quark mass. The results of [16] indicate that the pseudocritical temperatures are $T_c = 211(5)$ MeV and $T_c = 193(7)$ MeV at respectively $\bar{m}^{\overline{\text{MS}}} \simeq 15\text{MeV}$ and $\bar{m}^{\overline{\text{MS}}} \simeq 8\text{MeV}$ in the two-flavor theory. An extrapolation to $\bar{m}^{\overline{\text{MS}}} = 0$ yields values between 160 MeV and 175 MeV for the critical temperature in the chiral limit [16]. See [17, 18] for other lattice studies of the transition in the two-flavor theory.

The dependence of T_c on the quark mass is sketched in Fig. 1. The expected domain of applicability of a chiral expansion around a point (T, m) for $T < T_c(m = 0)$ is also indicated by the shaded region. We have performed two scans in temperature at constant renormalized quark mass, indicated by the dots on the horizontal lines in Fig. 1. Most of the ensembles considered here thus correspond to the crossover region. Son and Stephanov have also made

¹ The possibility considered to be the ‘standard scenario’ is that it is a second order phase transition in the 3d $O(4)$ universality class.

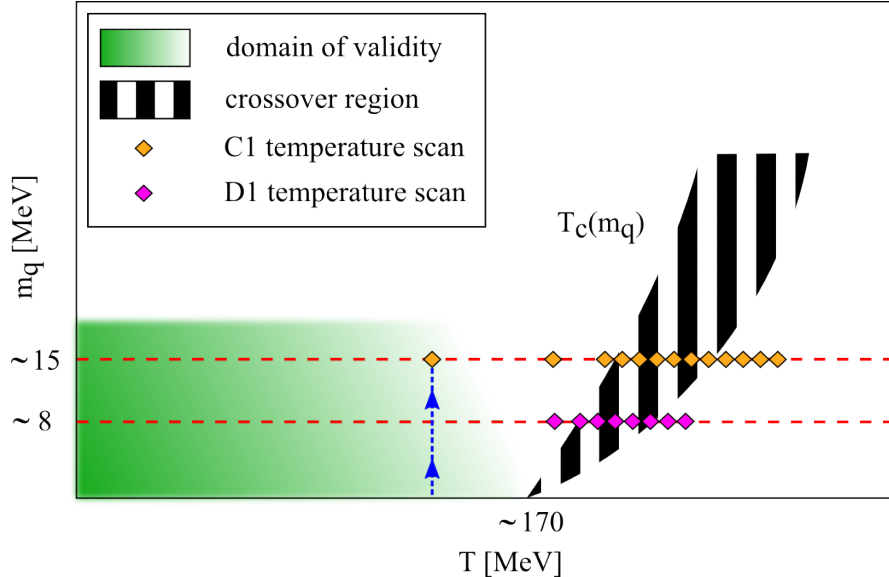


FIG. 1: Sketch of the domain of validity of the chiral effective field theory in the quark mass vs. temperature plane. The expansion is represented by the blue arrowed vertical line. The quark mass on the vertical axis is understood to be $\overline{m}^{\overline{\text{MS}}}$. The value of the critical temperature at the chiral limit $T_c(0) \simeq 170$ is taken from [16].

predictions for the scaling of the pion-sector observables [14] assuming a second-order phase transition,

$$f_\pi^2 \sim u^2 \sim t^\nu, \quad m_\pi^2 \sim m t^{\beta-\nu}, \quad (3)$$

where $t = (T_c - T)/T_c$ and β, ν are the standard critical exponents. These scaling predictions are meant to hold as long as $m_\pi \ll m_\sigma \ll T \simeq T_c$, with m_σ the inverse correlation length in the scalar channel. We will not be able to test these predictions, since it turns out that at the simulated quark masses, the system still exhibits a very smooth crossover. We point out, however, that all observables considered here are well defined for any temperature and any quark mass; this is in particular true for the estimators of the quantity $u(T)$ introduced above. It is the interpretation of the quantity $u(T)$ as the velocity of a quasiparticle that is uncertain.

The relatively strong dependence of the pseudocritical temperature on the quark mass tends to reduce the domain of applicability of the chiral expansion at fixed T . For instance, we clearly observe that the scaling $m_\pi^2 \propto m$ is violated at $T \simeq 180$ MeV. Instead the screening pion mass increases (sic!) as the quark mass is reduced from 15 MeV to 8 MeV. A plausible explanation is that at the smaller quark mass, the system is already entering the crossover region, where the chiral expansion breaks down.

We have found it useful to introduce the following ‘effective chiral condensate’ based on the Gell-Mann–Oakes–Renner (GOR) relation,

$$\langle \bar{\psi}\psi \rangle_{\text{GOR}} \equiv -\frac{f_\pi^2 m_\pi^2}{m}. \quad (4)$$

By construction it has the property that it tends to the actual chiral condensate when $m \rightarrow 0$; it is of order m above T_c , and thereby an order parameter with respect to chiral

symmetry. We remark that none of the observables considered here requires the use of a lattice action preserving chiral symmetry.

The goals of the lattice calculation presented here are the following:

1. test the validity of the chiral expansion around $(T, m = 0)$ and compute the pion quasiparticle velocity $u(T)$;
2. test the chiral expansion around $(T = 0, m = 0)$;
3. investigate the behavior of m_π , f_π and other quantities around the crossover, where no obvious expansion applies.

The corresponding results are the following:

1. The result for two estimators of the pion velocity is displayed in Fig. 7. The reasonable agreement of the two estimators observed up to $T \simeq 190$ MeV is a successful test of the validity of the chiral expansion. It therefore appears likely that the estimator $u_f(T \simeq 150 \text{ MeV}) = 0.88(2)$ for $\bar{m}^{\overline{\text{MS}}} = 15$ MeV does indeed provide a valid estimate of the pion quasiparticle velocity. The value indicates that there is a significant departure from unity, corresponding to a violation of boost invariance through the presence of the thermal medium. It shows that, although the hadron resonance gas model prediction for the thermodynamic potential $(e - 3p)/T^4$ [5] and the charge fluctuations agree well with lattice results [4, 6], the properties of the in-medium excitations can be shifted appreciably from their $T = 0$ counterparts.

The ability to extract the dispersion relation from Euclidean quantities rests on the dominance of the pion quasiparticle contribution in the axial charge correlator and in the pseudoscalar density correlator. In an attempt to test this dominance explicitly, we performed a reconstruction of the spectral function based on the Maximum Entropy Method (MEM). Having investigated the dependence of the result on the default model which is input to the method, we conclude that we cannot demonstrate the presence of a peak structure corresponding to the pion quasiparticle in the spectral function. However, quite model-independently the spectral weight is concentrated within $0 \leq \omega \lesssim 2.5T$. The spectral weight integrated over this interval is correspondingly robust and agrees with the quantity $(f_\pi/u_f)^2$, which it should if the pion quasiparticle indeed dominates the correlator.

2. Concerning the second goal, we find that at $T \simeq 150$ MeV, the static screening pion mass and the associated decay constant f_π have changed only by about 5% from their $T = 0$ values. Also the mass of the pion quasiparticle turns out to be very close to the $T = 0$ pion mass. These observations are in agreement with the predictions of the chiral expansion around the point $(m = 0, T = 0)$ [19]. Only a little higher up in temperature, the decay constant f_π and the correlation length m_π^{-1} fall off rapidly, a behavior no longer described by the chiral expansion.

3. Fig. 6 shows the behavior of the effective condensate defined via the GOR relation. This quantity, in spite of being a chiral order parameter, varies remarkably slowly throughout the crossover region. Fig. 8 displays our results for m_π/T and f_π/T as a function of temperature for two different quark masses; the temperature has been rescaled in units of the quark-mass dependent crossover temperature. Within the accuracy of the data, hardly any quark mass dependence is observed. These observations indicate that we are still deep in the crossover region and far from the chiral regime, where one expects a rapid fall-off of the condensate when $T \xrightarrow{\leq} T_c$ and an abrupt rise of m_π just above T_c .

The paper is structured as follows. In section II, we rederive relation (1) by exploiting chiral Ward identities between Euclidean QCD correlation functions. In the process, we also derive the exact spectral sum rule (2). Section III contains the description of the lattice data and the extraction of the pion quasiparticle velocity, as well as the comparison with chiral predictions. Section IV presents a study of the Euclidean-time dependent correlators using the MEM method. Finally, we give an outlook of how this investigation could be fruitfully extended.

II. CHIRAL WARD IDENTITIES IN THE THERMAL FIELD THEORY

We consider Euclideanized QCD with two flavors of degenerate quarks on the space $S^1 \times \mathbb{R}^3$, with the Matsubara cycle S^1 of length $\beta \equiv 1/T$. We label the Euclidean time direction as ‘0’, while the direction 1, 2 and 3 are of infinite extent; we write $x_\perp \equiv (x_1, x_2)$. Unexplained notation follows [20]. The Dirac field is a flavor doublet, for instance $\bar{\psi}(x) = (\bar{u}(x) \ \bar{d}(x))$.

We define the vector current, axial current and the pseudoscalar density as

$$V_\mu^a(x) = \bar{\psi}\gamma_\mu\frac{\tau^a}{2}\psi(x), \quad A_\mu^a(x) = \bar{\psi}\gamma_\mu\gamma_5\frac{\tau^a}{2}\psi(x), \quad P^a(x) = \bar{\psi}(x)\gamma_5\frac{\tau^a}{2}\psi(x). \quad (5)$$

where $a \in \{1, 2, 3\}$ is an adjoint $SU(2)_{\text{isospin}}$ index and τ^a is a Pauli matrix. The PCAC (partially conserved axial current) relation reads

$$\partial_\mu A_\mu^a(x) = 2mP^a(x), \quad (6)$$

where m is the common mass of the up and down quark. Eq. (6) is valid in any on-shell correlation function. The Ward identities for two-point functions (valid for all x ; see appendix A) that follow from the partial conservation of the axial current are

$$\langle A_\nu^a(0)\partial_\mu A_\mu^b(x) \rangle = 2m\langle A_\nu^a(0)P^b(x) \rangle \quad (7)$$

where we assume zero isospin chemical potential ($\langle V_\mu^a \rangle = 0 \ \forall a, \mu$), and

$$\langle P^a(0)\partial_\mu A_\mu^b(x) \rangle = -\frac{\delta^{ab}}{2}\langle \bar{\psi}\psi \rangle\delta^{(4)}(x) + 2m\langle P^a(0)P^b(x) \rangle. \quad (8)$$

A. Correlators in the massless theory

Space-time symmetries imply the following form for the $\langle P \mathbf{A} \rangle$ correlator,

$$\int dx_0 \langle P^a(0)\mathbf{A}^b(x) \rangle = \delta^{ab}g(r)\mathbf{e}_r, \quad r = |\mathbf{x}|, \quad \mathbf{e}_r = \frac{\mathbf{x}}{r}. \quad (9)$$

Integrating Eq. (8) over $\int_0^\beta dx_0 \int_{|\mathbf{x}|<R} d^3x$, using the form (9) and Gauss’s theorem, we get

$$g(r) = -\frac{\langle \bar{\psi}\psi \rangle}{8\pi r^2}. \quad (10)$$

This static correlator is thus fully determined by the chiral WI. Integrating Eq. (9) over an $x_3 = \text{constant}$ plane, one obtains²

$$\int dx_0 d^2x_\perp \langle A_3^a(x) P^b(0) \rangle = -\frac{\delta^{ab}}{4} \text{sign}(x_3) \langle \bar{\psi}\psi \rangle, \quad m = 0. \quad (11)$$

A second correlator can also be determined exactly in the massless theory. Indeed, for $x_0 \neq 0$ we have

$$\partial_0 \int_{r < R} d^3x \langle P^a(0) A_0^b(x) \rangle = - \int_{S_R} d\boldsymbol{\sigma} \cdot \langle P^a(0) \mathbf{A}^b(x) \rangle. \quad (12)$$

We assume that, when $\langle P^a(0) \mathbf{A}^b(x) \rangle$ is expanded in a Fourier series in x_0 , the non-constant modes fall off faster than $1/r^2$. If we then take the limit $R \rightarrow \infty$, using Eq. (9–10) we obtain

$$\partial_0 \int d^3x \langle P^a(0) A_0^b(x) \rangle = \delta^{ab} \frac{\langle \bar{\psi}\psi \rangle}{2\beta}. \quad (13)$$

Thus, since $\langle P^a(0) A_0^a(x) \rangle$ is odd in x_0 and in particular vanishes at $x_0 = \beta/2$,

$$\int d^3x \langle P^a(0) A_0^b(x) \rangle = \delta^{ab} \frac{\langle \bar{\psi}\psi \rangle}{2\beta} \left(x_0 - \frac{\beta}{2} \right). \quad (14)$$

B. Correlators at small quark mass: the pion decay constant and the GOR relation

The power law found in Eqs. (9–10) shows that P couples to a massless screening particle. The main idea in the following is to obtain the residue of the poles in the chiral limit, where they are determined by chiral Ward identities, and to use those at small but finite quark mass.

At finite quark mass, we expect³

$$\int dx_0 d^2x_\perp \langle A_3^a(x) P^b(0) \rangle \stackrel{|x_3| \rightarrow \infty}{=} \delta^{ab} \text{sign}(x_3) c(m) \exp(-m_\pi |x_3|), \quad (15)$$

with $c(0) = -\frac{1}{4} \langle \bar{\psi}\psi \rangle$ in view of Eq. (11). Since the PCAC relation (6) implies

$$\partial_3 \int dx_0 d^2x_\perp \langle A_3^a(x) P^b(0) \rangle = 2m \int dx_0 d^2x_\perp \langle P^a(0) P^b(x) \rangle, \quad (16)$$

we learn from (15) that close to the chiral limit,

$$\int dx_0 d^2x_\perp \langle P^a(0) P^b(x) \rangle = \delta^{ab} \frac{\langle \bar{\psi}\psi \rangle m_\pi}{8m} \exp(-m_\pi |x_3|). \quad (17)$$

² This last equation can also be obtained directly by integrating (8) over a ‘slab’ $\{x ||x_3| < y_3\}$ for some positive y_3

³ This equation defines m_π .

This equation shows that the correlation function of the pseudoscalar density admits a pole at m_π with residue $\frac{m_\pi^2 \langle \bar{\psi}\psi \rangle}{4m}$. Consequently, since the scalar propagator is $\frac{\exp(-m_\pi r)}{4\pi r}$ in three dimensions, we can write

$$\int dx_0 \langle P^a(0) P^b(x) \rangle \stackrel{r \rightarrow \infty}{=} \delta^{ab} \frac{m_\pi^2 \langle \bar{\psi}\psi \rangle}{4m} \frac{\exp(-m_\pi r)}{4\pi r}. \quad (18)$$

Now returning to Eq. (15), multiplying both sides by $2m$ and using the PCAC relation shows that close to the chiral limit,

$$\int dx_0 d^2 x_\perp \langle A_3^a(x) A_3^b(0) \rangle \stackrel{|x_3| \rightarrow \infty}{=} -\delta^{ab} \frac{m \langle \bar{\psi}\psi \rangle}{2m_\pi} \exp(-m_\pi |x_3|). \quad (19)$$

We know that the correlator $\int dx_0 \langle P^a(0) \mathbf{A}^a(x) \rangle$ is non-zero at $m = 0$; therefore the coupling of P to the Goldstone boson cannot vanish at $m = 0$ — consistently with Goldstone's theorem. Since the residue at the pion pole in the correlator (18) cannot diverge in the chiral limit, we conclude that $m_\pi^2 \sim m$.

The scaling of m_π with the quark mass motivates the definition of f_π (for any value of the quark mass) via

$$\int dx_0 d^2 x_\perp \langle A_3^a(x) A_3^b(0) \rangle = \frac{\delta^{ab}}{2} f_\pi^2 m_\pi e^{-m_\pi |x_3|}, \quad |x_3| \rightarrow \infty. \quad (20)$$

Comparison with the chiral prediction (19) shows that

$$f_\pi^2 m_\pi^2 = -m \langle \bar{\psi}\psi \rangle, \quad m \rightarrow 0, \quad (21)$$

in particular f_π has a finite, non-vanishing limit when $m \rightarrow 0$ as long as $\langle \bar{\psi}\psi \rangle$ is finite.

C. Spectral functions

Relation (14) shows that the pseudoscalar density and the axial charge density couple to a (real-time) massless excitation in the chiral limit. The goal is now to compute the dispersion relation of this excitation for small quark masses and spatial momenta.

We recall the relation between the spectral function and the Euclidean correlator for the following cases,

$$\delta^{ab} G_P(x_0, \mathbf{k}) \equiv \int d^3 x e^{-i\mathbf{k} \cdot \mathbf{x}} \langle P^a(0) P^b(x) \rangle = \delta^{ab} \int_0^\infty d\omega \rho_P(\omega, k) \frac{\cosh(\omega(\beta/2 - x_0))}{\sinh(\omega\beta/2)}, \quad (22)$$

$$\delta^{ab} G_{AP}(x_0, \mathbf{k}) \equiv \int d^3 x e^{-i\mathbf{k} \cdot \mathbf{x}} \langle P^a(0) A_0^b(x) \rangle = \delta^{ab} \int_0^\infty d\omega \rho_{AP}(\omega, k) \frac{\sinh(\omega(\beta/2 - x_0))}{\sinh(\omega\beta/2)}, \quad (23)$$

$$\delta^{ab} G_A(x_0, \mathbf{k}) \equiv \int d^3 x e^{-i\mathbf{k} \cdot \mathbf{x}} \langle A_0^a(0) A_0^b(x) \rangle = \delta^{ab} \int_0^\infty d\omega \rho_A(\omega, k) \frac{\cosh(\omega(\beta/2 - x_0))}{\sinh(\omega\beta/2)}. \quad (24)$$

The PCAC relation (6) implies

$$2m \rho_P(\omega, 0) = -\omega \rho_{AP}(\omega, 0), \quad (25)$$

$$\omega \rho_A(\omega, 0) = 2m \rho_{AP}(\omega, 0). \quad (26)$$

Equation (14), which is an exact expression in the chiral limit, shows that

$$\rho_{\text{AP}}(\omega, 0) = -\frac{\langle \bar{\psi}\psi \rangle}{2}\delta(\omega) \quad (m = 0). \quad (27)$$

Since $P(x)$ and $A_0(x)$ couple to a massless excitation at $m = k = 0$, they must also couple to an excitation when m and k are small but finite. In the following we assume that the imaginary part of the pole is negligible compared to its real part. An analysis in the hydrodynamic framework supports this assumption [15], as well as the chiral expansion around $T = 0$ [11]. We thus write the ansatz

$$\rho_{\text{P}}(\omega, k) = \text{sign}(\omega)C(k^2)\delta(\omega^2 - \omega_{\mathbf{k}}^2) + \dots \quad (28)$$

for the spectral function of the pseudoscalar density. We must have $\omega_{\mathbf{k}} \rightarrow 0$ when $m, k \rightarrow 0$ and the function $C(k^2)$ is the residue of the pole in ω^2 and is non-vanishing when $m_\pi, k \rightarrow 0$. We now show that the dispersion relation is of the form

$$\omega_{\mathbf{k}}^2 = u^2(m_\pi^2 + \mathbf{k}^2) + \mathcal{O}((\mathbf{k}^2)^2). \quad (29)$$

The key observation is that we know the static correlator, Eq. (18); it is proportional to a three-dimensional scalar propagator. The static correlator can be expressed in terms of the spectral function as follows (see for instance [21]),

$$\begin{aligned} \int dx_0 \langle P^a(0) P^b(x) \rangle &= 2\delta^{ab} \lim_{\epsilon \rightarrow 0} \int \frac{d^3k}{(2\pi)^3} e^{i\mathbf{k}\cdot\mathbf{x}} \int_0^\infty \frac{d\omega}{\omega} e^{-\epsilon\omega} \rho_{\text{P}}(\omega, k) \\ &= \delta^{ab} \int \frac{d^3k}{(2\pi)^3} e^{i\mathbf{k}\cdot\mathbf{x}} \frac{C(k^2)}{\omega_{\mathbf{k}}^2} + \dots \end{aligned} \quad (30)$$

Comparing with Eq. (18), we see that $\omega_{\mathbf{k}}^2$ must be proportional to $m_\pi^2 + \mathbf{k}^2$. Calling the proportionality factor u^2 , we have proved Eq. (29) and we then have

$$C(k^2) = -\frac{\langle \bar{\psi}\psi \rangle^2 u^2}{4f_\pi^2} \quad (31)$$

in the limit of small m_π and k . Relations (25–26) now lead to

$$\rho_{\text{AP}}(\omega, 0) = -\frac{\omega_{\mathbf{0}} \langle \bar{\psi}\psi \rangle}{2} \delta(\omega^2 - \omega_{\mathbf{0}}^2) + \dots, \quad (32)$$

$$\rho_{\text{A}}(\omega, 0) = \text{sign}(\omega) f_\pi^2 m_\pi^2 \delta(\omega^2 - \omega_{\mathbf{0}}^2) + \dots \quad (33)$$

D. An exact sum rule for $\rho_{\text{A}}(\omega, q)$

In appendix A, we show that the chiral Ward identities, together with the ultraviolet properties of the axial current correlator, imply the following exact sum rule for the axial current spectral function

$$\int_{-\infty}^{\infty} d\omega \, \omega \, \rho_{\text{A}}(\omega, \mathbf{k}) \Big|_0^T = -m \langle \bar{\psi}\psi \rangle \Big|_0^T. \quad (34)$$

This equation is valid at vanishing chemical potential, but for any quark mass; it is to be compared to the corresponding sum rule in the vector channel ($\langle V_0 V_0 \rangle$, [22, 23]),

$$\int_{-\infty}^{\infty} d\omega \, \omega \, \rho_V(\omega, \mathbf{k}) \Big|_0^T = 0. \quad (35)$$

The symbol $\{\dots\} \Big|_0^T$ means that the zero-temperature contribution is subtracted. The subtraction is necessary to make the integral over frequency convergent. One easily checks that the pion-quasiparticle contribution to $\rho_A(\omega, 0)$ given in (33) and the $T = 0$ pion contribution satisfy the sum rule (34).

The sum rules (34) and (35) are complementary to the sum rules derived in [24] in the massless theory. For $m = 0$, Eq. (34–35) are consistent with the sum rule ‘II-L’ given in [24] upon subtracting the $T = 0$ contributions.

E. Expressing u^2 in terms of static quantities

The parameter u can be obtained from $G_A(x_0, \mathbf{0})$, at sufficiently small quark mass, by noting that

$$\omega_0^2 = \frac{\partial_0^2 G_A(x_0, \mathbf{0})}{G_A(x_0, \mathbf{0})} \Big|_{x_0=\beta/2} = -4m^2 \frac{G_P(x_0, \mathbf{0})}{G_A(x_0, \mathbf{0})} \Big|_{x_0=\beta/2} \quad (36)$$

The chiral Ward identities allow one to express $\partial_0^2 G_A(x_0, \mathbf{0})$ in terms of f_π , m_π and ω_0 . Using the spectral function (33), one obtains

$$\partial_0^2 G_A(x_0, \mathbf{0}) = \frac{f_\pi^2 m_\pi^2 \omega_0}{2} \frac{\cosh(\omega_0(\beta/2 - x_0))}{\sinh(\omega_0 \beta/2)}. \quad (37)$$

Inserting expression (37) into Eq. (36) yields the following algebraic equation for u ,

$$u \sinh(u m_\pi \beta/2) = \frac{f_\pi^2 m_\pi}{2G_A(\beta/2, \mathbf{0})}. \quad (38)$$

This equation provides a way to extract the velocity u from Euclidean correlation functions. It is valid throughout the shaded region in Fig. 1, i.e. for sufficiently small quark masses and for all $T < T_c(m = 0)$. In the massless case, this relation is equivalent to the result of Son and Stephanov [15],

$$u^2 = \frac{f_\pi^2}{\int_0^\beta dx_0 \, G_A(x_0, \mathbf{0})} \quad (m = 0). \quad (39)$$

The axial susceptibility appearing in the denominator of (39) however contains an ultraviolet divergence at any non-vanishing quark mass. It is therefore not practical to use in lattice calculations.

III. LATTICE CALCULATION

In this section we describe the numerical lattice QCD calculation of the temperature dependent parameters u and m_π that characterize the pion dispersion relation; see Eq. (29). All

finite temperature correlation functions are measured on a set of dynamical gauge ensembles with two mass degenerate quark flavors covering a temperature range $150 \leq T \leq 235$ MeV. We use the plaquette gauge action and the $O(a)$ improved Wilson fermion action with a non-perturbatively determined c_{sw} coefficient [25]. The configurations were generated using the MP-HMC algorithm [26, 27] following the implementation described in [28] based on Lüscher's DD-HMC package [29].

Two scans in temperature were carried out on lattices of size 16×32^3 , where the short direction is interpreted as time and therefore $T = 1/(16a)$ and the spatial extent is $L = 32a$. The gluon fields have periodic boundary conditions in all directions, while the quark fields are periodic in space and antiperiodic in time. The temperature is varied by varying the bare coupling g_0^2 , which amounts to varying the lattice spacing at fixed 'aspect ratio' $LT = 2$. The scale setting was done via the Sommer parameter [30]. We use a quadratic interpolation of $\log(r/a)$ based on the data given in [31] to relate the lattice spacings at two values of the bare coupling. The absolute scale setting, a/fm , is done using the value $r_0 = 0.503(10)$ fm [31].

The two scans correspond to two quark masses of respectively about 8 MeV and 15 MeV, where the bare quark mass is tuned to keep the renormalized quark mass constant (see Fig. 2). The quark mass is given in the $\overline{\text{MS}}$ scheme at a scale $\mu = 2\text{GeV}$ for which we used the renormalization factors $Z_A(g_0^2)$ and $Z_P = 0.5184(53)$ from [31] as well as the conversion factor from the Schrödinger Functional (SF) to the $\overline{\text{MS}}$ scheme, which is $0.968(20)$ [31].

We use the standard definition for the quark mass that comes from the PCAC relation [32, 33]

$$m_{\text{PCAC}}(x_3) = \frac{1}{2} \frac{\int dx_0 d^2 x_\perp \left\langle \partial_3^{\text{imp}} A_3^{a,\text{imp}}(x) P^a(0) \right\rangle}{\int dx_0 d^2 x_\perp \langle P^b(x) P^b(0) \rangle}, \quad x_\perp = (x_1, x_2), \quad (40)$$

where in the improvement process

$$A_\mu^a \longrightarrow A_\mu^{a,\text{imp}} = A_\mu^a + ac_A \partial_\mu^{\text{imp}} P^a. \quad (41)$$

The derivative $\partial_\mu^{\text{imp}}$ is the improved lattice discretized version of the derivative following [34]. The non-perturbatively calculated coefficient c_A was taken from [35]. Notice that since the PCAC relation is an operator identity, we are free to choose the direction in which we define the quark mass – any dependence on the direction must therefore amount to a discretization error. On our lattices, the spatial direction is longer, so measuring along these directions we obtain a longer plateau and thus, smaller errors. The extraction is carried out by performing a fit to a constant in the range where a plateau is observed. Within errors the PCAC masses measured in the time and in spatial directions agree.

The two scans, called C1 and D1, have respectively pseudocritical temperatures of $T_c = 211(5)$ MeV and $T_c = 193(7)$ MeV [16]. For instance, in Fig. 2, we observe that in scan C1, our renormalized quark mass in physical units is approximately constant up to $T = 211$ MeV where the phase transition to the deconfined phase is estimated to occur. This means that the ensembles presented in Tabs. I and II follow to a good approximation 'lines of constant physics' and can be interpreted as temperature scans at fixed quark mass.

Statistical errors on the observables are calculated using the jackknife method. In plots, only the statistical error from our simulations are displayed; the error from renormalization factors and the scale setting uncertainty should be added in quadrature to obtain the full uncertainty.

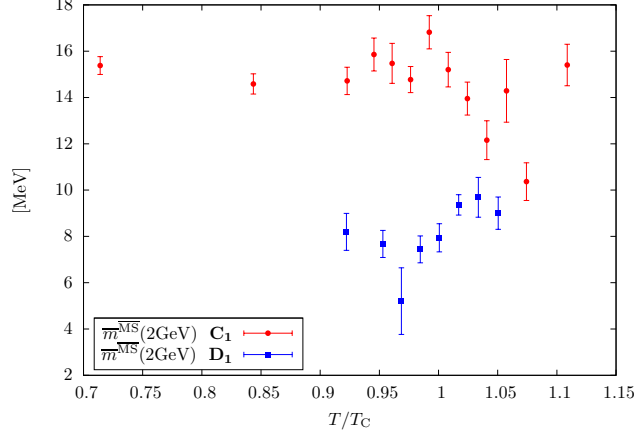


FIG. 2: Renormalized quark mass in physical units in the $\overline{\text{MS}}$ scheme for both temperature scans (C1 and D1). For the C1 scan, $T_c = 211(5)$ MeV, and for D1, $T_c = 193(7)$ MeV.

A. Basic observables

In this section we describe the calculation of the following observables:

- the midpoint of the axial charge correlator in the time direction, $G_A(\beta/2, \mathbf{0})$;
- the midpoint of the pseudoscalar correlator in the time direction, $G_P(\beta/2, \mathbf{0})$;
- the screening pion mass m_π ;
- the screening pion decay constant f_π .

The values of the correlators $G_A(\beta/2, \mathbf{0})$ and $G_P(\beta/2, \mathbf{0})$ at $x_0 = \beta/2$ are displayed in Fig. 3. While the former only exhibits a mild temperature dependence, the latter quantity is strongly temperature dependent. Since $\partial_0^2 G_A(x_0) = -4m^2 G_P(x_0)$, this observation means that the axial charge correlator becomes flatter as a function of x_0 . It shows that the spectral density $\rho_A(\omega, 0)$ must concentrate around the origin as the temperature rises.

1. Extraction of m_π

In order to extract the ‘screening’ pion mass, we compute the symmetrized pseudoscalar-pseudoscalar screening Euclidean correlator along a spatial direction,

$$\delta^{ab} G_P^s(x_3) = \int dx_0 d^2 x_\perp \langle P^a(x) P^b(0) \rangle, \quad G_P^s(x_3) \stackrel{|x_3| \rightarrow \infty}{\sim} e^{-m_\pi |x_3|} \quad (42)$$

At long distances, it is dominated by the lowest lying state with pseudoscalar quantum numbers, which we call the ‘screening pion’. In practice, a two state fit to the correlation function via Levenberg-Marquardt’s method [36] is performed using an ansatz of the form

$$G_P^s(x_3) = A_1^P \cosh[m_1^P(x_3 - L/2)] + A_2^P \cosh[m_2^P(x_3 - L/2)]. \quad (43)$$

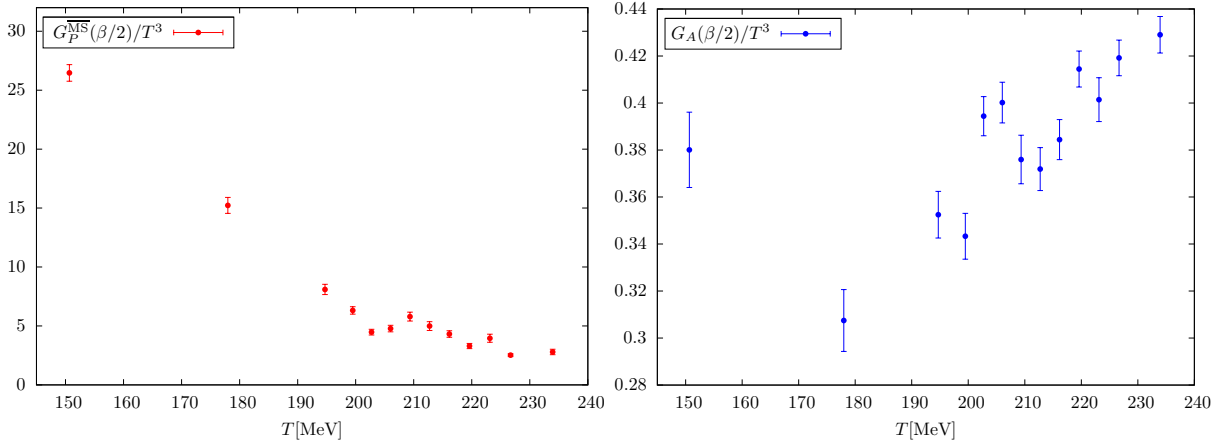


FIG. 3: Midpoints of the renormalized correlators $G_A(x_0)$ and $G_P(x_0)$. The former was renormalized via multiplication with Z_A^2 , the latter via multiplication with Z_P^2 as well as the conversion factor from the SF to the $\overline{\text{MS}}$ scheme at the scale $\mu = 2\text{GeV}$. All data from the C1 temperature scan.

To initialize the fit-routine we use as input parameter for $m_1^P \doteq m_\pi$ an averaged value of the ‘coshmass’ $m_{\text{cosh}}(x_3)$ defined as the positive root of the following equation,

$$\frac{G_P^s(x_3)}{G_P^s(x_3 + a)} = \frac{\cosh[m_{\text{cosh}}(x_3 + a/2)(x_3 - L/2)]}{\cosh[m_{\text{cosh}}(x_3 + a/2)(x_3 + a - L/2)]}; \quad (44)$$

In order to be sure that the ground state is isolated one can repeat the fit to the correlation function for different fit windows, leaving out points that are furthest away from the middle point $x_3 = L/2$ of the correlator. We choose for the m_π result quoted in table IV a value corresponding to a small $\chi^2/\text{d.o.f}$ which is stable under small variations of the fit window. The result for m_π obtained in this way is close, in value and in its uncertainty, to m_{cosh} around $x_3 = L/2$; see Fig. 4.

The temperature dependence of m_π is illustrated in the left panel of Fig. 5. We observe that the correlation length in the thermal medium becomes shorter as the temperature increases, and is about half as long at the crossover as it is at zero-temperature.

2. Extraction of f_π

We extract f_π from the correlation function

$$\delta^{ab} G_A^s(x_3) = \int dx_0 d^2x_\perp \left\langle A_3^{a,\text{imp}}(x) A_3^{b,\text{imp}}(0) \right\rangle \Big|_{x_3 \rightarrow \infty} \stackrel{\delta^{ab}}{=} \frac{f_\pi^2 m_\pi}{2} e^{-m_\pi x_3} \quad (45)$$

Because of the noisier behavior of this correlator, it turns out that the fit to this correlation function is more stable using a 1-state-fit rather than a 2-state-fit. Since G_A^s is symmetric around $x_3 = L/2$ we use an ansatz of the form

$$G_A^s(x_3) = A_1^A \cosh[m_1^A(x_3 - L/2)]. \quad (46)$$

For stability reasons we put $m_1^A = m_\pi$ by hand since this quantity is already known from the G_P^s -fit. This reduces the number of parameters to one. By repeating the procedure for

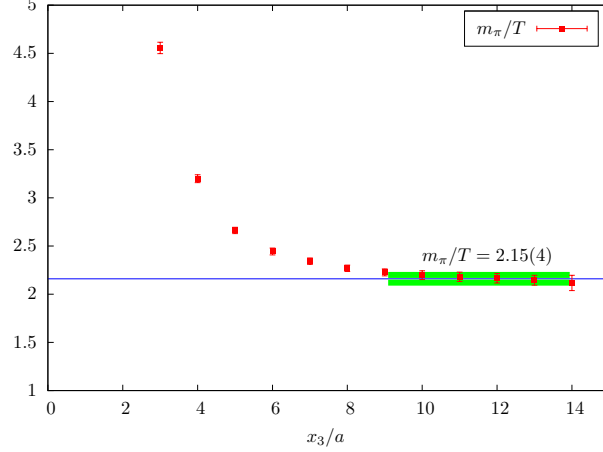


FIG. 4: Example of an effective-mass plot showing $m_{\text{cosh}}(x_3 + a/2)$ for the pseudoscalar density two-point function in the x_3 -direction in the C1 scan at $T = 150$ MeV. The result of the fit to the correlation function is represented by a (1σ) band. Here the chosen fit-window was 26, which corresponds to ignoring the three points closest to each operator, and the (uncorrelated) $\chi^2/\text{d.o.f}$ amounts to 0.05.

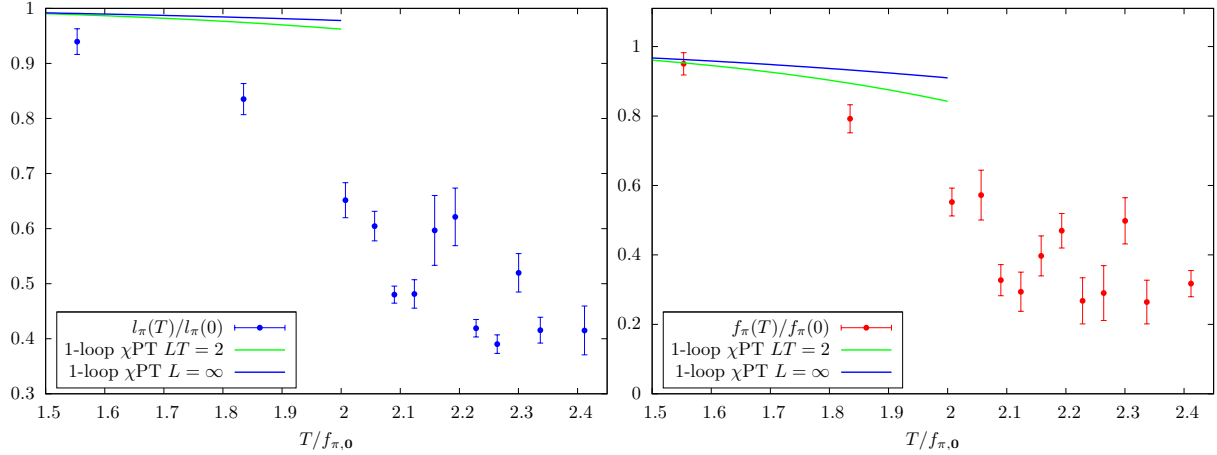


FIG. 5: Inverse screening mass $l_{\pi} \equiv m_{\pi}^{-1}$ (left) and screening pion ‘decay constant’ (right) in the C1 scan, divided by the same quantity at $T \simeq 0$ extracted from the A5 ensemble. The displayed error bars represent the statistical errors originating from the ensembles of the C1 scan and from ensemble A5.

different fit windows as explained above, we select the final value for A_1^A by choosing a fit which has a low $\chi^2/\text{d.o.f}$. The relation between A_1^A and f_{π} reads

$$f_{\pi}^2 = \frac{2 A_1^A \sinh(m_{\pi}L/2)}{m_{\pi}}. \quad (47)$$

The temperature dependence of f_{π} in the C1 temperature scan is displayed in the right panel of Fig. 5. We observe a reduction of f_{π} as the temperature increases, reaching a value of about one third its zero-temperature value around the crossover.

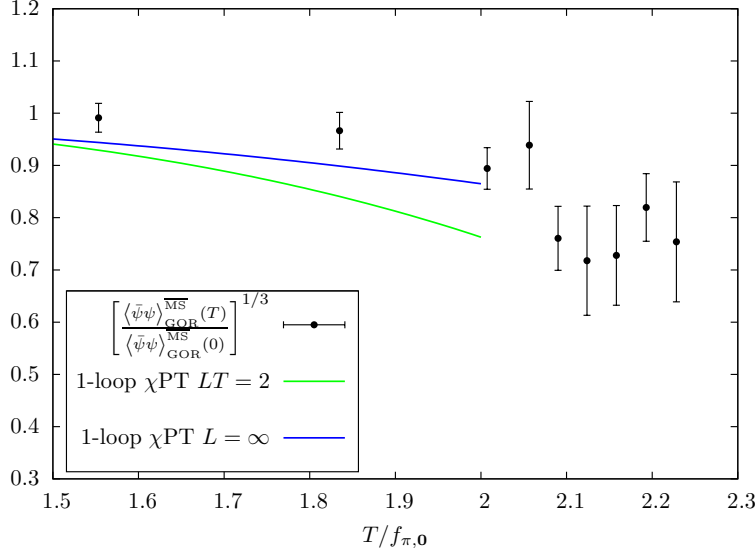


FIG. 6: Effective chiral condensate defined from the GOR relation, divided by its $T = 0$ counterpart, in the temperature scan C1. In addition, the predictions of [19] both for the infinite volume limit and for our finite lattice volume are displayed. The temperature is given in units of the zero-temperature decay constant $f_{\pi,0}$.

3. Chiral condensate $\langle \bar{\psi}\psi \rangle$

Using the Gell-Mann–Oakes–Renner relation [37], one can define an effective chiral condensate as follows (see Eq. 4),

$$\langle \bar{\psi}\psi \rangle_{\text{GOR}}^{\overline{\text{MS}}} = -\frac{f_{\pi}^2 m_{\pi}^2}{\overline{m}^{\overline{\text{MS}}}}. \quad (48)$$

Since $m_{\pi} \sim T$ and $f_{\pi} \sim m$ above T_c , $\langle \bar{\psi}\psi \rangle_{\text{GOR}}^{\overline{\text{MS}}}$ is of order m above T_c ; at high temperatures, it is expected to grow as mT^2 .

The behavior of the effective chiral condensate is displayed in Fig. 6. We find it to be weakly temperature dependent around T_c . It illustrates how smooth the crossover is at the quark mass used in the temperature scan C1: around $T = 200$ MeV, $|\langle \bar{\psi}\psi \rangle_{\text{GOR}}^{\overline{\text{MS}}}|^{1/3}$ only appears to be about 10% lower than at zero temperature.

B. Lattice estimators for the pion velocity

We showed that, at sufficiently small quark mass, the axial charge correlator is dominated by a light quasiparticle and that its mass ω_0 is given by Eq. (36). With $\omega_0 = um_{\pi}$, the following estimator for u can be defined,

$$u_m^2 = -\frac{4m^2}{m_{\pi}^2} \frac{G_P(x_0, \mathbf{0})}{G_A(x_0, \mathbf{0})} \Big|_{x_0=\beta/2}. \quad (49)$$

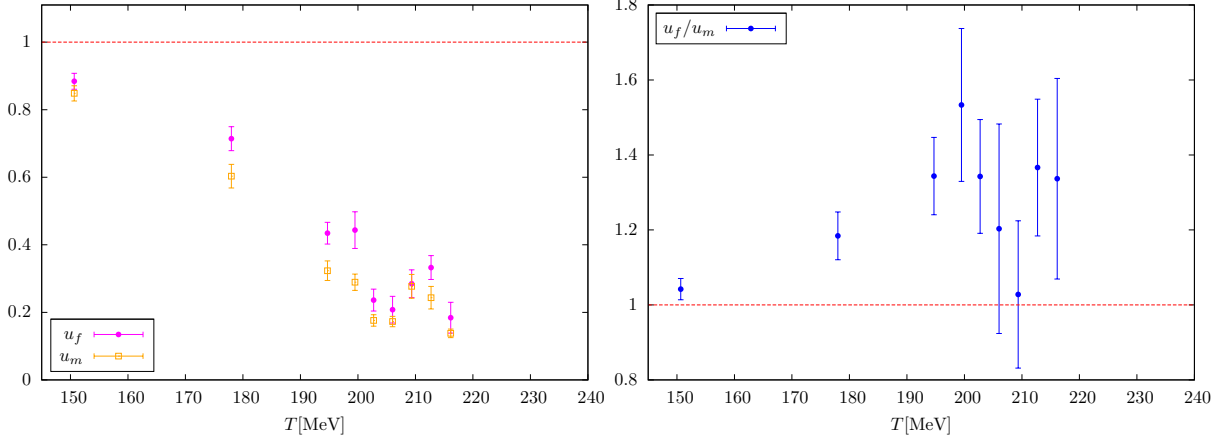


FIG. 7: Left: The two estimators of the pion velocity in the C1 scan. Right: Ratio of the estimators, which serves as a test of the chiral prediction (37).

We introduce a second estimator for u based on Eq. (38),

$$u_f \sinh(u_f m_\pi \beta/2) = \frac{f_\pi^2 m_\pi}{2G_A(\beta/2, \mathbf{0})}. \quad (50)$$

It should be noticed that the pion velocity is a renormalization group invariant quantity and thus, does not require any renormalization. The results for u_f and u_m are shown in Fig. 7. We observe a significant reduction of both quantities from unity, pointing to a pion ‘velocity’ well below the speed of light. However, whether the interpretation is valid for $T \gtrsim 160$ MeV is questionable.

One way to test the validity of the chiral effective theory predictions is the following. The chiral EFT makes a prediction for $G_P(\beta/2)$ in terms of f_π , m_π and $G_A(\beta/2)$; see Eq. (36–37). Testing whether $u_f/u_m = 1$ is equivalent to testing this prediction. It is worth noting that at high temperatures, well in the deconfined phase, $u_m = O(m^2/T^2)$, while $u_f = O(m/T)$, so that u_f/u_m is expected to grow with temperature. In the lattice data displayed in the right panel of Fig. 7 we indeed observe that u_f/u_m grows above unity. Thus it is at the lowest-temperature ensemble in the C1 temperature scan that we are most confident in the interpretation of u_f as the pion quasiparticle velocity.

C. The $T = 0$ ensemble and test of chiral perturbation theory predictions

In addition to the analysis of thermal ensembles, it is interesting to compute the same observables on a corresponding zero-temperature ensemble. One reason is that we obtain the reference values of ω_0 , m_π and f_π at $T = 0$; the thermal modification of these quantities can be compared with the predictions of chiral perturbation theory [19, 38]. A second, practical reason is to check the validity of our estimators for $u(T)$, since $\lim_{T \rightarrow 0} u(T) = 1$. We therefore analyze the CLS ensemble labelled A5 in [31]. All ensemble parameters coincide with the lowest-temperature ensemble in the C1 scan; the only difference is the lattice extent in the time direction, which is 64 instead of 16. The bare parameters and the computed observables are summarized in Tab. III.

In contrast to the thermal ensembles, here we are able to directly extract the mass of the pion propagating in the temporal direction, which we denote by ω_0 . It is extracted by fitting to a constant the coshmass of the pseudoscalar-pseudoscalar correlator, where a clear plateau is observed. The pion decay constant $f_{\pi,0}$ is calculated by fitting the amplitude of the axial charge correlator $G_A(x_0)$. The effective quark condensate $|\langle\bar{\psi}\psi\rangle_{\text{GOR},0}^{\overline{\text{MS}}}|^{1/3}$ given in Tab. III follows the definition (48), except that m_π was replaced by ω_0 and f_π by $f_{\pi,0}$.

We find that the extraction of the pseudoscalar mass in the spatial and in the temporal direction give the same answer within two standard deviations. The estimators u_f and u_m are both compatible with unity within two standard deviations; this adds to our confidence that the estimators work as expected in practice.

We use m_π and f_π to normalize the corresponding quantities at finite temperature in Fig. 5. This allows for the most natural comparison of the predictions of one-loop chiral perturbation theory [19], an expansion around $(T = 0, m = 0)$, with the lattice data. We display both the prediction for the infinite-volume system and for the finite-volume system; details are given in appendix B. At the lowest temperature in the C1 scan ($T \simeq 150$ MeV), the prediction agrees very well with the lattice result for f_π . The central value of the correlation length m_π^{-1} lies somewhat lower than the corresponding chiral prediction, but still within two standard deviations. However, on the next ensemble, at $T \simeq 177$ MeV, the lattice data clearly deviates from the chiral prediction. From this temperature onwards, both m_π and f_π deviate substantially from their $T = 0$ counterparts. One-loop chiral perturbation theory predictions at $T \gtrsim 170$ MeV appear to be unreliable.

We remark that the prediction for $f_\pi(T)/f_\pi(0)$ does not involve directly the relation between the quark mass and the pion screening mass. The GOR-condensate, however, does; it is compared to the chiral prediction in Fig. 6. Here the quantities combine to give a result which is only mildly temperature-dependent. Correspondingly the chiral prediction lies numerically quite close to the data points. The prediction for the GOR condensate seems to be more robust than the predictions for m_π and f_π taken separately; it works, at our current level of accuracy, essentially up to the transition temperature.

We can in principle compare the pion quasiparticle mass, computed as $\omega_0(T) = u(T)m_\pi(T)$, with the two-loop predictions of chiral perturbation theory [11, 12]. At $T = 150$ MeV in the C1 scan, we find

$$\frac{\omega_0(T)}{\omega_0(0)} = 0.97(4), \quad (51)$$

where $\omega_0(T = 0) = 294(4)$ MeV. Thus the thermal shift of the pion quasiparticle mass appears to be very small. At the same temperature, but at the physical quark mass, the corresponding quantity is predicted to be about 0.86 at the two-loop level [11]; we note that there is a change in the sign of $\frac{\omega_0(T)}{\omega_0(0)} - 1$ between the one-loop and the two-loop result at this temperature. Clearly one expects the thermal effect on ω_0 to be smaller at heavier quark masses. Thus the lattice results are not obviously inconsistent with the chiral prediction. We postpone a more detailed comparison of lattice results for the quantity ω_0 (and indeed ω_k) with chiral perturbation theory to a future study.

The relative success of the one-loop chiral prediction for the thermal effect on the ‘chiral’ quantities m_π , f_π and $\langle\bar{\psi}\psi\rangle_{\text{GOR}}$ at

$$T = 150 \text{ MeV} \simeq 0.7T_c \quad (\bar{m}^{\overline{\text{MS}}} \simeq 15 \text{ MeV}) \quad (52)$$

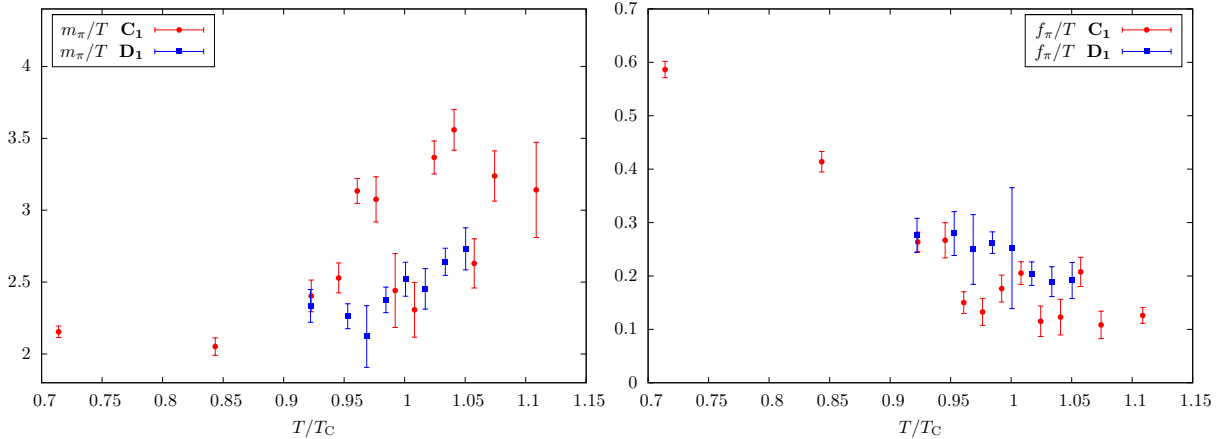


FIG. 8: Temperature dependence of the pion screening mass and the associated decay constant, for two quark masses. The temperature is given in units of the pseudocritical temperature at the corresponding quark mass.

is somewhat unexpected when one considers that the energy density, say, for physical quark masses is completely dominated by hadrons more massive than pions [5, 38]. The surprise at the quark mass used here is, in a sense, that chiral quantities are still affected below the 10% level by the thermal effects. However, the effect of the thermal medium increases rapidly above $T = 150$ MeV.

D. Quark mass dependence of m_π and f_π around the pseudocritical temperature

The scan D1 at the light quark mass is more concentrated around the pseudocritical temperature. Therefore we can only discuss the quark mass dependence of the observables discussed so far in the crossover region; see Fig. 8. We find that, if m_π/T and f_π/T are viewed as a function of T/T_c , where T_c is the quark-mass dependent pseudocritical temperature, the quark mass dependence is very mild. In this respect we are far from the deeply chiral regime where the screening pion mass exhibits a sudden steep rise at T_c , from a low value below T_c of order \sqrt{m} .

A look at Tab. IV–V shows that the effective condensate appears to be quite insensitive to the quark mass up to $T = 195$ MeV, which corresponds to the pseudocritical temperature at the lower quark mass. In other words, the GOR relation is satisfied within the uncertainties, in spite of the fact that, at fixed temperature, the pion mass m_π does not decrease with the quark mass between scan C1 and scan D1.

IV. SPECTRAL FUNCTION RECONSTRUCTION USING THE MAXIMUM ENTROPY METHOD

So far we have concentrated on computing the properties of the pion quasiparticle indirectly from spatial correlation functions, relying on the chiral effective theory. Given the lattice extent is larger in the spatial directions, this approach has the advantage that masses and amplitudes can be calculated quite accurately from the data. For example determining the pion pole mass from the temporal correlation function is not possible given only $N_t/2 = 8$

points on the available lattice ensembles, while we achieve an accuracy of roughly 4% on the same ensembles in the spatial direction, i.e. with $N_s/2 = 16$ points. Since all quantities of interest here are accessible from the spectral function, an alternative approach is to study the behavior of the spectral functions underlying the temporal correlation functions.

To achieve this one has to invert the kernel $K(x_0, \omega) = \frac{\cosh(\omega(\beta/2 - x_0))}{\sinh(\omega\beta/2)}$, see Eqs. (22)-(24). Inverting this type of equation in order to extract the spectral function is a typical ill-posed problem. One commonly adopted procedure to compute spectral functions from lattice correlation functions is the Maximum Entropy Method (MEM) [39–46]. In this method the guiding principle for the selection of the most likely solution given the finite number of lattice data points with errors and an input default model is Bayesian statistical inference.

We adopt the implementation of MEM presented in [47–49], which is based on Brian’s algorithm. Defining the modified kernel

$$\tilde{K}(x_0, \omega) \equiv \tanh(\omega\beta/2)K(x_0, \omega), \quad (53)$$

the spectral function is parametrized as

$$\rho(\omega) = m(\omega) \exp(f(\omega)), \quad (54)$$

where $m(\omega)$ is an input default model and $f(\omega)$ is expanded in a basis of functions that depends on the choice of the kernel \tilde{K} . Due to the divergence of $K(x_0, \omega)$ as $\omega \rightarrow 0$, the redefinition (53) ensures a stable behavior of MEM around $\omega \sim 0$, while retaining the large frequency behavior of the original kernel. This is one choice for the modified kernel, however different redefinitions are possible and have been used in the past [45, 46].

The choice of input default model plays a crucial role in any spectral function reconstruction using MEM and currently poses the largest source of error. It enters into the definition of the Shannon-Jaynes entropy term

$$S[\rho] = \alpha \int_0^\infty \frac{d\omega}{2\pi} \left[\rho(\omega) - m(\omega) - \rho(\omega) \log \left(\frac{\rho(\omega)}{m(\omega)} \right) \right], \quad (55)$$

and, in the Bayesian language, is part of the prior information H . The parameter α weights the relative importance of the data and the prior knowledge. Given this term and the standard likelihood function $L[\rho] = \chi^2/2$, the most probable spectral function $\rho(\omega)$ underlying the lattice correlator G can be obtained by maximizing the conditional probability

$$P[\rho|GH] = \exp(S[\rho] - L[\rho]). \quad (56)$$

There is a lot of freedom in choosing the default model $m(\omega)$ for the entropy term. However, it can be shown [39] that, given precise enough data, MEM will produce a unique solution, if it exists, regardless of the default model. Unfortunately, in practice the data is not accurate enough to ensure this property and it is not a priori clear how a specific choice of default model impacts the obtained solution. Therefore great care must be taken in MEM analyses to check the dependence on the default model by repeating the analysis with several sufficiently different classes of them. Any stable features accross all results should then be safe to interpret in terms of physics.

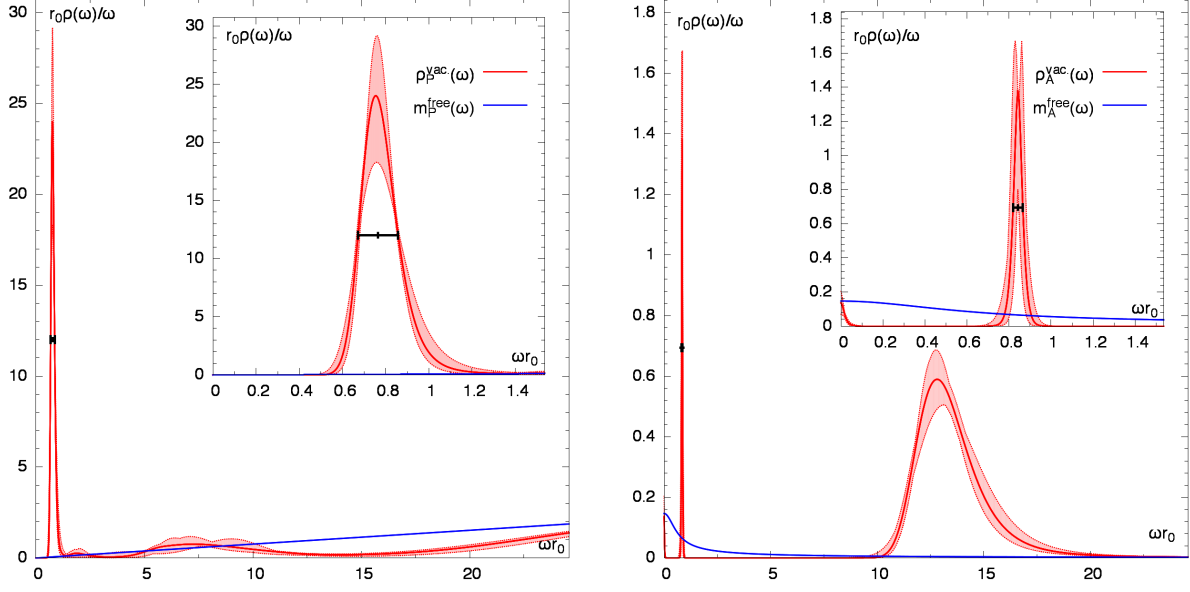


FIG. 9: The MEM reconstruction of the vacuum P (left) and A_0 (right) channel spectral functions. In both cases a free theory inspired default model $m_{A/P}^{\text{free}}(\omega)$ is used as prior information for the MEM analysis. The black error bars indicate the half-maximum width and midpoint, which we define to give m_π and its error. The broad peak structure at large frequencies is understood as lattice artifact. The quoted error bands represent the spread of spectral functions obtained in a jackknife analysis.

A. Choice of default models and vacuum spectral functions

In this study we will choose default models corresponding to the infinite temperature limit on the one hand and the zero temperature case on the other. The former corresponds to a system of non-interacting quarks, and the analytically known spectral functions [50, 51] provide a default model. Specifically we choose

$$m_P^{\text{free}}(\omega) \sim \omega^2 \tanh(\omega/2T) \quad \text{and} \quad m_A^{\text{free}}(\omega) \sim \tanh(\omega/2T), \quad (57)$$

even though the proportionality constants are known analytically, in the actual analysis we freely vary them as an additional crosscheck. These default models are essentially featureless and leave the most ‘freedom’ to the MEM analysis to extract excitations. For the zero temperature limit the A5 lattice ensemble plays a crucial role, as it enables the reconstruction of vacuum spectral functions on a large lattice with very accurate data. We therefore reconstruct the spectral functions $\rho_P^{\text{vac}}(\omega)$ and $\rho_A^{\text{vac}}(\omega)$ using the free default models Eq. (57) and subsequently define them to be the ‘vacuum’ default models

$$m_P^{\text{vac}}(\omega) = \rho_P^{\text{vac}}(\omega) \quad \text{and} \quad m_A^{\text{vac}}(\omega) = \rho_A^{\text{vac}}(\omega), \quad (58)$$

to be used in the analysis of the thermal correlators.

In Fig. 9 we show the resulting spectral functions over frequency in units of the reference scale r_0 , along with their respective free default models in the P (left) and the A_0 (right) channels. To estimate the statistical uncertainties, the MEM analysis is repeated on a set of jackknife samples, the given error band shows the spread of the resulting spectral functions.

In both cases we observe the emergence of a narrow peak in the low frequency region and a broad peak structure at large frequencies. The second peak structure is to be understood as a lattice artifact, as the free lattice spectral functions also exhibit such a structure [51]. In both channels we observe a clear separation between the low frequency spectrum dominated region and the lattice cut-off region. In the P case this separation is located roughly around $\omega a \sim 0.5 - 1.0$, while in the A_0 channel we observe a separation window from $\omega a \sim 0.25$ through to $\omega a \sim 1.5$. In the next step we associate the low frequency peak structure with the pion. To read off its mass from the spectral functions obtained by the MEM analysis, we calculate the peak maximum on the unsampled result. The mass and ‘resolution error’ are then given by the width of the peak at half-maximum and its midpoint (black error bars in Fig. 9). Combining the resulting values with the lattice spacing $a = 0.0818\text{fm}$ we obtain $m_\pi^P = 300(36)\text{ MeV}$ and $m_\pi^A = 331(9)\text{ MeV}$. Comparing these values to those obtained from fitting the spatial and temporal correlators in the P channel tabulated in Tab. III, we find very good agreement for the result originating from the P channel, while the result extracted from the A_0 channel is larger. The likely explanation is the observed peak located around $\omega \simeq 0$ in the A_0 channel in Fig. 9 (right). This contribution to the spectral function is then compensated, in the MEM reconstruction, by a shift of the pion peak position to larger frequencies.

The clear statistical stability of the vacuum spectral functions obtained on the A5 lattice ensemble using the free default models in Fig. 9, motivates us to choose the average spectral function (red lines in Fig. 9) as default models for the MEM reconstruction of the finite temperature spectral functions.

B. Thermal spectral functions in the A_0 channel and f_π^2/u^2

Following the discussion of Sec. II C, using Eqs. (31) and (33) the integral over the spectral function in the A_0 channel can be linked to f_π^2/u^2 ,

$$\rho_A(\omega) = \frac{f_\pi^2 m_\pi}{2u} \delta(\omega - \omega_0) \quad \Longrightarrow \quad \mathcal{A}(\Lambda) \equiv 2 \int_0^\Lambda \frac{d\omega}{\omega} \rho_A(\omega) = \frac{f_\pi^2}{u^2}, \quad (59)$$

where Λ is a scale separation parameter between the low and large frequency regions. While the details of the spectral functions themselves, like peak positions and widths, are generally very sensitive to the input default model, the area under these spectral functions in a given interval is more robust.

In the following, we reconstruct the thermal spectral functions in the A_0 channel and compute the area according to Eq. (59). For every available ensemble we choose $m_A^{\text{free}}(\omega)$, $m_A^{\text{vac}}(\omega)$ and $m_P^{\text{vac}}(\omega)$ as input default models. Using these three models we cover a range of inputs that go from a very smooth, featureless ($m_A^{\text{free}}(\omega)$) to a rather specific ($m_A^{\text{vac}}(\omega)$) model. We show the default models in the left panel of Fig. 10, whereby we rescaled $m_P^{\text{vac}}(\omega) = \rho_P^{\text{vac}}(\omega, m_P^{\text{free}}(\omega))$ by a factor $1/c = 20$ for readability. In the middle and the right panel, we show the resulting thermal spectral functions $r_0 \rho_A(\omega, \mathbf{0})/\omega$ and their statistical error bands for the $6/g_0^2 = 5.20$ and $6/g_0^2 = 5.30$ ensembles. Note once more that the bare parameters of the $6/g_0^2 = 5.20$ ensemble of the C1 scan are identical to those of the $N_t = 64$ reference ensemble. Already in this case we observe the free default model does not lead to a sharp peak result in the finite temperature ensemble. Instead the resulting spectral function exhibits a broad peak centered around $\omega \simeq 0$. Reconstructing the spectral function using

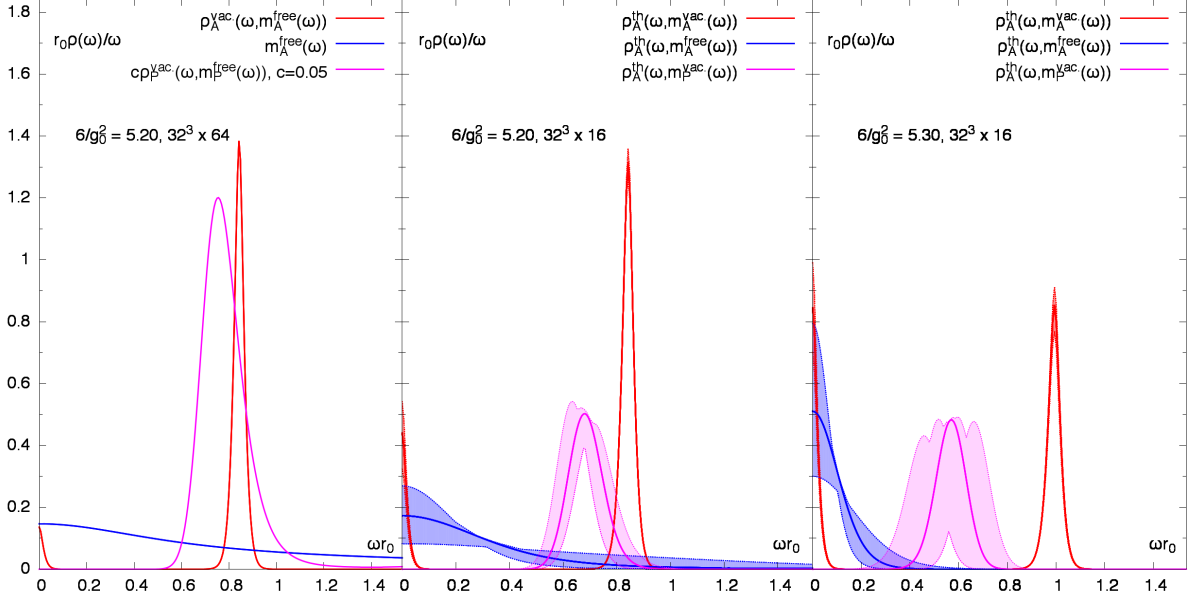


FIG. 10: Reconstruction of the spectral function ρ_A of the axial charge at finite temperature and vanishing spatial momentum. The notation $\rho_A = \rho_A^T(\omega, m(\omega))$ emphasizes the default-model dependence. Left: The three input default models used for the reconstruction of the thermal spectral function. Middle: The MEM reconstruction of the spectral function on the $6/g_0^2 = 5.20$ ensemble of the C1 scan for all three default models. The quoted error bands represent the spread of spectral functions obtained in a jackknife analysis. Right: The corresponding MEM results for the $6/g_0^2 = 5.30$ ensemble of the C1 scan.

the peaked default models on the other hand leads to low frequency peaks, as observed in the vacuum case. Comparing the results at $6/g_0^2 = 5.20$ and $6/g_0^2 = 5.30$ we observe a drop in the peak amplitudes for the peak-type default models; and a more narrow peak for the results obtained from the free default model.

In the next step we compute the area under the spectral functions as prescribed in Eq. (59). To do so we first analyze the dependence on the cut-off parameter Λ at $6/g_0^2 = 5.20$ and $N_t = 16$, the result is shown in Fig. 11(left). The errors shown in this plot originate from a jackknife procedure to calculate the integral over the spectral function up to the cut parameter Λ . For the two peak-type default models we observe a clear plateau, i.e. cutoff-independence, for values of $r_0\Lambda$ above about 1.2, which in both cases is slightly above the peak region. This plateau is seen to be stable up until $r_0\Lambda \simeq 8$ for the P -type and $r_0\Lambda \simeq 10$ for the A_0 -type default model. For the free default model we observe a cut-dependence up to values of $r_0\Lambda \simeq 4.3$, the subsequent plateau is stable up to $r_0\Lambda \simeq 10$. In the following, we choose a suitable value for Λ by determining a local minimum of the spectral function in the interval $1.2 \lesssim r_0\Lambda \lesssim 10$.

Using the same default models (in units of temperature), we repeat the MEM-reconstruction and subsequent determination of f_π^2/u^2 for all available lattice ensembles. Rescaling the latter quantity by T^2 , we compare the results in the C1 scan with those obtained using static quantities in Fig. 11 (right panel). As before, the quoted errors originate from a jackknife analysis in the MEM reconstruction and we use the three default models described above. As an example, we give our MEM results for f_π/u on the $N_t = 64$ and

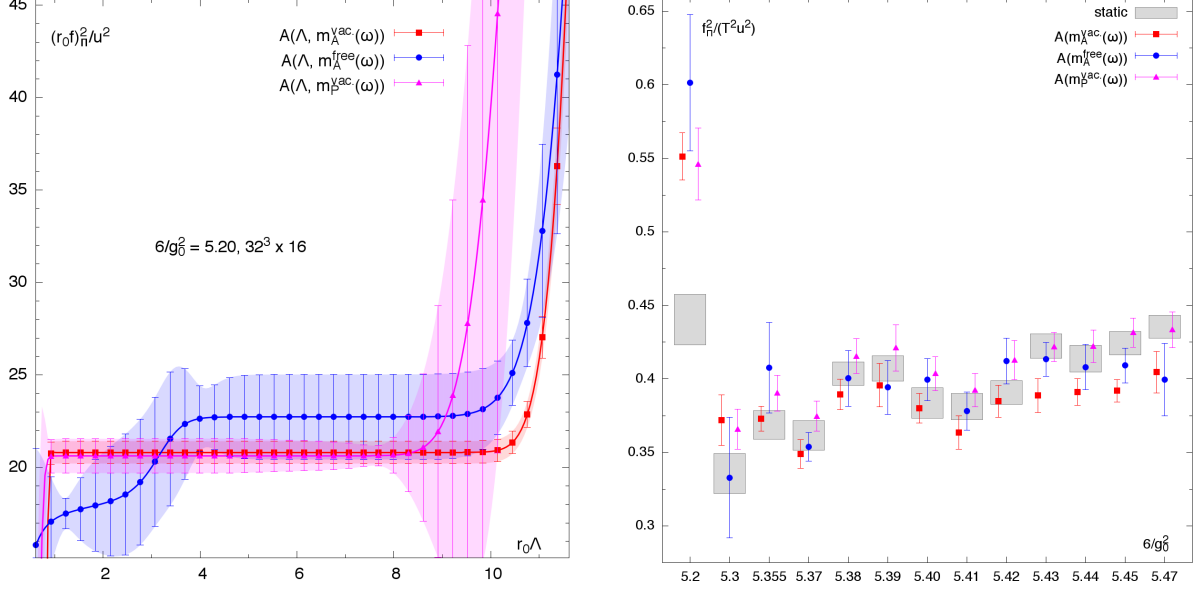


FIG. 11: Left: The area $\mathcal{A}(\Lambda, m(\omega))$ for different values of the cut-parameter Λ on the $6/g_0^2 = 5.20$ ensemble of the C1 scan obtained from a MEM reconstruction using all three default models $m(\omega)$. We observe a clear plateau and therefore separation region. Right: The area $\mathcal{A}(\Lambda, m(\omega))$ for all available lattice ensembles in units of T^2 , compared to the results of Sec. III for $f_\pi^2/(T^2 u_f^2)$, which make use of static quantities.

$N_t = 16$ ensembles at $6/g_0^2 = 5.20$,

$$\left(\frac{f_\pi}{u}\right)^{T=37\text{MeV}} = 110(23)\text{MeV} \quad \text{and} \quad \left(\frac{f_\pi}{u}\right)^{T=150\text{MeV}} = 113(19)(32)(24)\text{MeV}, \quad (60)$$

where we quote the average value over all MEM-results and the errors from the A_0 -vacuum, A_0 -free and P -vacuum default models respectively.

The grey shaded areas in Fig. 11 (right) denote the results obtained from the analysis of Sec. III, which uses static correlation functions. Overall we find good agreement between the MEM based results and the approach of Sec. III. In the lowest-temperature ensemble of the C1 scan, the MEM results overshoot the static results. A possible reason is that in Sec. III, the spectral function ρ_A is assumed to be given by a single ‘delta function’, while the result of the MEM reconstruction exhibits (for each default model) a more complicated spectral weight distribution. It is at the lowest temperature that the comparison is most sensitive to this difference. We note however that the agreement improves if one uses the estimator u_m instead of u_f in the quantity f_π/u computed in Sec. III.

V. OUTLOOK

This work represents a step towards understanding the degrees of freedom dictating the static correlations and the dynamical properties of QCD in its low-temperature phase. We have computed the two temperature-dependent parameters that determine the pion quasiparticle dispersion relation (see Eq. (1)). The results are compared to (mostly one-loop) predictions of chiral perturbation theory. The methods introduced in this paper can

be applied to ensembles with a quark content closer to the real world: it would be very interesting to compute all observables considered here on QCD ensembles with up, down and strange quarks at their physical masses (see the recent [52]). In order to test the functional form of the pion quasiparticle dispersion relation (1), it would be very interesting to analyze data at non-vanishing spatial momentum \mathbf{k} .

The results presented in this paper are still subject to cutoff and finite volume effects, which have not been investigated. Especially the latter can still be quite sizeable since the ensembles at our disposal have a rather small spatial extent with an aspect ratio of $LT = 2$. Currently the set of ensembles is extended to aspect ratios of $LT = 3$ and 4. Cutoff effects are presumably small, since with $1/aT = 16$ we are at the state-of-the-art concerning the temporal extent at the transition temperature. However, a systematic study of cutoff effects would also be desirable.

In order to test the $T = 0$ chiral effective theory predictions more stringently, additional simulations at temperatures 100-150 MeV are required at lighter quark masses. The comparisons with the available two-loops calculations in chiral perturbation theory [11, 12] could then be done systematically.

Appendix A: Chiral Ward identities for two-point functions & a sum rule

The isovector vector and axial-vector currents, as well as the pseudoscalar density were defined in Eq. (5). We use the Euclidean field theory method to derive the axial Ward identities [20]. We assume that all chemical potentials are set to zero. It is useful to recall some of the space-time transformation properties of these local operators. Under the Euclidean time reversal tranformation ($x'_0 = -x_0$, $\mathbf{x}' = \mathbf{x}$), we have

$$A_0^{a'}(x') = A_0^a(x), \quad A_k^{a'}(x') = -A_k^a(x), \quad P^{a'}(x') = -P^a(x), \quad (\text{A1})$$

while under ($x' = -x$)

$$A_\mu^{a'}(x') = -A_\mu^a(x), \quad P^{a'}(x') = P^a(x). \quad (\text{A2})$$

We also note that V_μ is odd under charge conjugation C , while P and A_μ are even.

The variations of the quark and antiquark fields under an infinitesimal, isovector, axial phase rotation read

$$\delta_A^a \psi(x) = \frac{1}{2} \tau^a \gamma_5 \psi(x), \quad \delta_A^a \bar{\psi}(x) = \bar{\psi}(x) \gamma_5 \frac{1}{2} \tau^a. \quad (\text{A3})$$

They lead to the following transformation of the composite operators,

$$\delta_A^a A_\mu^b(x) = -i\epsilon^{abc} V_\mu^c(x), \quad \delta_A^a P^b(x) = \frac{\delta^{ab}}{2} \bar{\psi} \psi, \quad (\text{A4})$$

For an axial transformation parameter $\alpha^a(x)$, the variation of the action is given by [53]

$$\delta S = \int d^4x \left(\partial_\mu \alpha(x)^a A_\mu^a(x) + \alpha(x)^a 2m P^a(x) \right). \quad (\text{A5})$$

In the path integral, the invariance of the integration measure under the transformation above leads to $\langle \delta \mathcal{O} \rangle = \langle \mathcal{O} \delta S \rangle$. In particular, if \mathcal{O} consists of one local field located at the point y ,

$$\alpha(y) \langle \delta_A^a \mathcal{O}(y) \rangle = \langle \mathcal{O}(y) \int d^4x \left(\partial_\mu \alpha(x) A_\mu^a(x) + \alpha(x) 2m P^a(x) \right) \rangle \quad (\text{A6})$$

In the following we set $\alpha(x) = e^{ikx}$ and consider several choices for \mathcal{O} . Choosing $\mathcal{O} = A_\nu^b$, we obtain

$$0 = ik_\mu \langle A_\nu^b(0) \int d^4x e^{ikx} A_\mu^a(x) \rangle + 2m \int d^4x e^{ikx} \langle A_\nu^b(0) P^a(x) \rangle. \quad (\text{A7})$$

Choosing instead $\mathcal{O} = P^b$, we obtain

$$\frac{1}{2} \delta^{ab} \langle \bar{\psi} \psi \rangle = ik_\mu \langle P^b(0) \int d^4x e^{ikx} A_\mu^a(x) \rangle + 2m \langle P^b(0) \int d^4x e^{ikx} P^a(x) \rangle. \quad (\text{A8})$$

These are the momentum-space versions of the Ward identities, while Eq. (7–8) are the position-space versions.

1. A sum rule for the spectral function of the axial charge density

Combining Eq. (A7) and (A8), one finds

$$k_\mu k_\nu \int d^4x e^{ikx} \langle A_\nu^b(0) A_\mu^a(x) \rangle = -m \delta^{ab} \langle \bar{\psi} \psi \rangle + 4m^2 \int d^4x e^{ikx} \langle P^b(0) P^a(x) \rangle. \quad (\text{A9})$$

Next we consider the difference of this relation at finite temperature and at zero temperature. The operator-product expansion indicates that the most singular contributions arise from dimension four operators. By power counting, all the correlators appearing in (A9) are then expected to be finite. More precisely, for large k_0 and finite quark mass, all correlators in (A9) are of order k_0^{-2} . The left-hand side of the equation has a finite contribution when $k_0 \rightarrow \infty$ given by the $\int d^4x e^{ikx} \langle A_0 A_0 \rangle|_0^T$ correlator, since it is multiplied by k_0^2 . On the right-hand side, the only surviving term is given by the condensate. The coefficient of the $\mathcal{O}(k_0^{-2})$ term of the $\int d^4x e^{ikx} \langle A_0^a(0) A_0^b(x) \rangle|_0^T$ correlator must thus equal $-m \delta^{ab} \langle \bar{\psi} \psi \rangle|_0^T$ and it cannot contain logarithms of k_0 . To convert this statement into a property of the spectral function, we use the spectral representation (see for instance [7])

$$\int d^4x e^{ikx} \langle A_0^b(0) A_0^a(x) \rangle|_0^T = \delta^{ab} \int_{-\infty}^{\infty} d\omega \frac{\omega}{\omega^2 + k_0^2} \rho_A(\omega, k)|_0^T. \quad (\text{A10})$$

The absence of logarithms in the coefficient of k_0^{-2} on the left-hand side of Eq. (A10)⁴ indicates that $\omega \rho_A(\omega, \mathbf{k})|_0^T$ is integrable. Expanding the integrand on the right-hand side of Eq. (A10) to order k_0^{-2} we then obtain

$$\int_{-\infty}^{\infty} d\omega \omega \rho_A(\omega, \mathbf{k})|_0^T = -m \langle \bar{\psi} \psi \rangle|_0^T. \quad (\text{A11})$$

⁴ This is confirmed by the two-loop calculation of [54]. The most singular OPE term for the left-hand side of Eq. (A10) comes from the longitudinal channel, and is denoted $\frac{k_0^2}{(k_0^2 + \mathbf{k}^2)^2} C_2^L O_2^L$ in [54]. In position space, the second derivative with respect to x_0 of this term is a contact term (plus terms of order $|x_0|$). It thus does not contribute to the spectral density at order ω^{-2} .

Appendix B: Chiral perturbation theory predictions for finite-temperature observables

The one-loop results of [19] for the finite-temperature and finite-size effects on the chiral observables can be written as

$$\frac{\mathcal{O}(T, L)}{\mathcal{O}(0, \infty)} = 1 - \nu_{\mathcal{O}} \frac{m_{\pi}^2}{f_{\pi}^2} \tilde{g}_1(m_{\pi}/T, m_{\pi}L), \quad (\text{B1})$$

$$\nu_{f_{\pi}} = 1, \quad \nu_{m_{\pi}} = -\frac{1}{4}, \quad \nu_{\langle \bar{\psi}\psi \rangle} = \frac{3}{2}, \quad (\text{B2})$$

$$\tilde{g}_1(x, y) = \frac{1}{(4\pi)^2} \sum_{n_1, n_2, n_3, n_4} \int_0^{\infty} d\lambda \lambda^{-2} \exp \left[-\lambda - \frac{1}{4\lambda} (y^2(n_1^2 + n_2^2 + n_3^2) + x^2 n_4^2) \right]. \quad (\text{B3})$$

On the right-hand side, m_{π} and f_{π} are understood to be the zero-temperature, infinite-volume quantities. The sum runs over four integers, where the term $(n_1, n_2, n_3, n_4) = (0, 0, 0, 0)$ is to be omitted. In addition to showing

$$\frac{f_{\pi}(T, \infty)}{f_{\pi}(0, \infty)}, \quad \frac{m_{\pi}(T, \infty)}{m_{\pi}(0, \infty)}, \quad \frac{\langle \bar{\psi}\psi \rangle(T, \infty)}{\langle \bar{\psi}\psi \rangle(0, \infty)}, \quad (\text{B4})$$

as a function of T , we also display the curves

$$\frac{f_{\pi}(T, 2/T)}{f_{\pi}(0, L_{\text{ref}})}, \quad \frac{m_{\pi}(T, 2/T)}{m_{\pi}(0, L_{\text{ref}})}, \quad \frac{\langle \bar{\psi}\psi \rangle(T, 2/T)}{\langle \bar{\psi}\psi \rangle(0, L_{\text{ref}})} \quad (\text{B5})$$

in Fig. (5, 6), where L_{ref} corresponds to the spatial linear size of the A_5 ensemble. In this way the finite size ($L = 2/T$) of the spatial volume in our thermal ensembles are taken into account in the comparison with the predictions of chiral perturbation theory.

Appendix C: Tables

$6/g_0^2$	κ	c_{sw}	a [fm]	T [MeV]	$Z_A(g_0^2)$	$\overline{m}^{\overline{\text{MS}}}$ [MeV]
5.20	0.13594	2.017147	0.0818(8)	150(1)	0.7703(57)	15.4(4)
5.30	0.13636	1.909519	0.0693(6)	177(2)	0.7784(52)	14.6(6)
5.355	0.13650	1.859618	0.0633(7)	194(2)	0.7826(49)	14.7(6)
5.37	0.13652	1.846965	0.0618(7)	199(2)	0.7838(48)	15.8(7)
5.38	0.13654	1.838739	0.0608(7)	203(2)	0.7845(48)	15.5(9)
5.39	0.13656	1.830676	0.0599(6)	206(2)	0.7853(48)	14.8(6)
5.40	0.13658	1.822771	0.0589(6)	209(2)	0.7860(47)	16.8(7)
5.41	0.13660	1.815019	0.0580(6)	213(2)	0.7868(47)	15.2(7)
5.42	0.13662	1.807416	0.0571(6)	216(2)	0.7875(46)	14.0(7)
5.43	0.13664	1.799958	0.0562(6)	219(2)	0.7882(46)	12.2(8)
5.44	0.13665	1.792642	0.0553(5)	223(2)	0.7889(45)	14.2(10)
5.45	0.13666	1.785462	0.0544(5)	226(2)	0.7896(45)	10.3(8)
5.47	0.13667	1.771499	0.0527(5)	234(2)	0.7910(44)	15.4(9)

TABLE I: Lattice parameters for the scan C1. All our finite-temperature lattices are 16×32^3 . The error on the lattice spacings and on the temperatures comes from interpolating a second order polynomial with the three known input values for r_0/a evaluated at $6/g_0^2 = 5.20, 5.30, 5.50$ [31]. The error shown on $\overline{m}^{\overline{\text{MS}}}$ includes neither the uncertainty of the renormalization constants nor the error due to the scale setting. The latter two sources of error combine to be about 0.4-0.5 MeV in the whole range of $6/g_0^2$.

$6/g_0^2$	κ	c_{sw}	a [fm]	T [MeV]	$Z_A(g_0^2)$	$\overline{m}^{\overline{\text{MS}}}$ [MeV]
5.30	0.13640	1.909519	0.0693(6)	177(2)	0.7784(52)	8.2(8)
5.32	0.13646	1.890703	0.0671(7)	183(2)	0.7800(51)	7.7(5)
5.33	0.13649	1.881590	0.0660(7)	186(2)	0.7808(50)	5.2(10)
5.34	0.13651	1.872665	0.0649(7)	189(2)	0.7815(50)	7.4(6)
5.35	0.13653	1.863922	0.0639(7)	192(2)	0.7823(49)	7.9(6)
5.36	0.13655	1.855357	0.0628(7)	195(2)	0.7830(49)	9.3(4)
5.37	0.13657	1.846965	0.0618(6)	199(2)	0.7838(48)	9.7(9)
5.38	0.13659	1.838739	0.0608(7)	203(2)	0.7845(48)	9.0(7)

TABLE II: Lattice parameters with lower quark mass (scan D1; the lattice size is 16×32^3 for each ensemble). The displayed errors have the same meaning as in Table I.

$6/g_0^2$	5.20
κ	0.13594
c_{sw}	2.017147
T [MeV]	37.7(4)
a [fm]	0.0818(8)
Z_A	0.7703(57)
$\overline{m}^{\overline{\text{MS}}}(\mu = 2\text{GeV})$ [MeV]	14.7(3)
m_π [MeV]	305(5)
f_π [MeV]	93(2)
$\left \langle\bar{\psi}\psi\rangle_{\text{GOR}}^{\overline{\text{MS}}}\right ^{1/3}(\mu = 2\text{GeV})$ [MeV]	364(7)
$\omega_{\mathbf{0}}$ [MeV]	294(4)
$f_{\pi,\mathbf{0}}$ [MeV]	97(3)
$\left \langle\bar{\psi}\psi\rangle_{\text{GOR},\mathbf{0}}^{\overline{\text{MS}}}\right ^{1/3}(\mu = 2\text{GeV})$ [MeV]	368(9)
u_f	0.96(2)
u_m	0.92(6)
u_f/u_m	1.04(4)
$\omega_{\mathbf{0}}/m_\pi$	0.96(2)

TABLE III: Summary of results for the 64×32^3 ensemble ‘A5’.

$T[\text{MeV}]$	$G_P^{\overline{\text{MS}}}(\beta/2)/T^3$	$G_A(\beta/2)/T^3$	$m_\pi(T)/T$	$f_\pi(T)/T$	$\left \langle\bar{\psi}\psi\rangle_{\text{GOR}}^{\overline{\text{MS}}}\right ^{1/3}/T$	u_f	u_m	u_f/u_m
150(1)	26.5(7)	0.38(2)	2.15(4)	0.59(2)	2.40(5)	0.88(2)	0.84(2)	1.04(3)
177(2)	15.2(7)	0.31(1)	2.05(6)	0.41(2)	1.98(6)	0.71(4)	0.60(3)	1.18(6)
194(2)	8.1(4)	0.35(1)	2.4(1)	0.26(2)	1.67(7)	0.43(3)	0.32(3)	1.3(1)
199(2)	6.3(3)	0.34(1)	2.5(1)	0.27(3)	1.7(1)	0.44(5)	0.29(2)	1.5(2)
203(2)	4.5(2)	0.394(8)	3.13(8)	0.15(2)	1.4(1)	0.24(3)	0.18(2)	1.3(2)
206(2)	4.8(3)	0.400(9)	3.1(2)	0.13(3)	1.3(2)	0.21(4)	0.17(2)	1.2(3)
209(2)	5.8(4)	0.38(1)	2.4(3)	0.18(3)	1.3(2)	0.28(4)	0.28(4)	1.0(2)
213(2)	5.0(4)	0.372(9)	2.3(2)	0.20(2)	1.4(1)	0.33(4)	0.24(3)	1.4(2)
216(2)	4.3(3)	0.384(8)	3.4(1)	0.12(3)	1.3(2)	0.18(5)	0.14(1)	1.3(2)
219(2)	3.3(2)	0.414(8)	3.6(1)	0.12(3)	1.4(3)	0.19(5)	0.09(1)	2.0(5)
223(2)	4.0(3)	0.401(9)	2.6(2)	0.21(3)	1.6(2)	0.32(4)	0.16(3)	2.0(3)
226(2)	2.5(1)	0.419(8)	3.2(2)	0.11(3)	1.3(2)	0.17(4)	0.074(9)	2.2(6)
234(2)	2.8(2)	0.429(7)	3.1(3)	0.13(1)	1.3(1)	0.19(2)	0.11(2)	1.6(3)

TABLE IV: Summary of numerical results for the temperature scan C1. All errors given here are statistical and the uncertainty from the renormalization constants is not included.

$T[\text{MeV}]$	$G_P^{\overline{\text{MS}}}(\beta/2)/T^3$	$G_A(\beta/2)/T^3$	$m_\pi(T)/T$	$f_\pi(T)/T$	$ \langle\bar{\psi}\psi\rangle_{\text{GOR}}^{\overline{\text{MS}}} ^{1/3}/T$	u_f	u_m	u_f/u_m
177(2)	14.9(10)	0.36(2)	2.3(1)	0.28(3)	2.0(2)	0.45(5)	0.27(4)	1.6(3)
183(2)	11.5(9)	0.35(1)	2.26(9)	0.28(4)	2.0(2)	0.46(7)	0.22(2)	2.0(3)
186(2)	8.6(9)	0.41(1)	2.1(2)	0.25(7)	2.1(4)	0.38(9)	0.13(3)	3(1)
189(2)	9.9(9)	0.37(1)	2.38(9)	0.26(2)	2.1(1)	0.42(3)	0.18(2)	2.3(3)
192(2)	7.4(5)	0.385(9)	2.5(1)	0.25(11)	2.0(6)	0.4(2)	0.15(2)	2.6(11)
195(2)	8.9(5)	0.369(8)	2.5(1)	0.20(2)	1.6(1)	0.33(4)	0.21(2)	1.6(2)
199(2)	8.2(7)	0.37(1)	2.64(9)	0.19(3)	1.7(2)	0.31(5)	0.19(2)	1.6(3)
203(2)	7.1(5)	0.39(1)	2.7(1)	0.19(3)	1.8(2)	0.30(5)	0.15(2)	2.0(4)

TABLE V: Summary of numerical results for the D_1 temperature scan. All errors given here are statistical and the uncertainty from the renormalization constants is not included.

Acknowledgments

We are grateful for the access to the zero-temperature ensemble used here, made available to us through CLS. We acknowledge the use of computing time for the generation of the gauge configurations on the JUGENE computer of the Gauss Centre for Supercomputing located at Forschungszentrum Jülich, Germany; the finite-temperature ensemble was generated within the John von Neumann Institute for Computing (NIC) project HMZ21. The correlation functions were computed on the dedicated QCD platform “Wilson” at the Institute for Nuclear Physics, University of Mainz. This work was supported by the *Center for Computational Sciences in Mainz* as part of the Rhineland-Palatinate Research Initiative and by the DFG grant ME 3622/2-1 *Static and dynamic properties of QCD at finite temperature*.

-
- [1] N. Brambilla, S. Eidelman, P. Foka, S. Gardner, A. Kronfeld, et al. (2014), 1404.3723.
 - [2] P. Braun-Munzinger, B. Friman, F. Karsch, K. Redlich, and V. Skokov, Nucl.Phys. **A880**, 48 (2012), 1111.5063.
 - [3] J. Stachel, A. Andronic, P. Braun-Munzinger, and K. Redlich (2013), 1311.4662.
 - [4] A. Bazavov et al. (HotQCD Collaboration), Phys.Rev. **D86**, 034509 (2012), 1203.0784.
 - [5] S. Borsanyi, Z. Fodor, C. Hoelbling, S. D. Katz, S. Krieg, et al., Phys.Lett. **B730**, 99 (2014), 1309.5258.
 - [6] S. Borsanyi, Z. Fodor, S. D. Katz, S. Krieg, C. Ratti, et al., JHEP **1201**, 138 (2012), 1112.4416.
 - [7] H. B. Meyer, Eur.Phys.J. **A47**, 86 (2011), 1104.3708.
 - [8] E. V. Shuryak, Phys.Rev. **D42**, 1764 (1990).
 - [9] J. Goity and H. Leutwyler, Phys.Lett. **B228**, 517 (1989).
 - [10] A. Schenk, Nucl.Phys. **B363**, 97 (1991).
 - [11] A. Schenk, Phys.Rev. **D47**, 5138 (1993).
 - [12] D. Toublan, Phys.Rev. **D56**, 5629 (1997), hep-ph/9706273.
 - [13] R. D. Pisarski and M. Tytgat, Phys.Rev. **D54**, 2989 (1996), hep-ph/9604404.
 - [14] D. T. Son and M. A. Stephanov, Phys. Rev. Lett. **88**, 202302 (2002), hep-ph/0111100.
 - [15] D. T. Son and M. A. Stephanov, Phys. Rev. **D66**, 076011 (2002), hep-ph/0204226.
 - [16] B. B. Brandt, A. Francis, H. B. Meyer, O. Philipsen, and H. Wittig (2013), 1310.8326.
 - [17] F. Burger et al. (tmfT), Phys.Rev. **D87**, 074508 (2013), 1102.4530.
 - [18] V. Boryakov, R. Horsley, S. Morozov, Y. Nakamura, M. Polikarpov, et al., Phys.Rev. **D82**, 014504 (2010), 0910.2392.
 - [19] J. Gasser and H. Leutwyler, Phys.Lett. **B184**, 83 (1987).
 - [20] M. Lüscher, S. Sint, R. Sommer, and H. Wittig, Nucl.Phys. **B491**, 344 (1997), hep-lat/9611015.
 - [21] H. B. Meyer, PoS **LAT08**, 017 (2008), 0809.5202.
 - [22] D. Bernecker and H. B. Meyer, Eur.Phys.J. **A47**, 148 (2011), 1107.4388.
 - [23] B. B. Brandt, A. Francis, H. B. Meyer, and H. Wittig, JHEP **1303**, 100 (2013), 1212.4200.
 - [24] J. I. Kapusta and E. V. Shuryak, Phys. Rev. **D49**, 4694 (1994), hep-ph/9312245.
 - [25] K. Jansen and R. Sommer (ALPHA collaboration), Nucl.Phys. **B530**, 185 (1998), hep-lat/9803017.
 - [26] M. Hasenbusch, Phys.Lett. **B519**, 177 (2001), hep-lat/0107019.

- [27] M. Hasenbusch and K. Jansen, Nucl.Phys. **B659**, 299 (2003), hep-lat/0211042.
- [28] M. Marinkovic and S. Schaefer, PoS **LATTICE2010**, 031 (2010), 1011.0911.
- [29] <http://luscher.web.cern.ch/luscher/DD-HMC/index.html> (2010).
- [30] R. Sommer, Nucl. Phys. **B411**, 839 (1994), hep-lat/9310022.
- [31] P. Fritzsche, F. Knechtli, B. Leder, M. Marinkovic, S. Schaefer, et al., Nucl.Phys. **B865**, 397 (2012), 1205.5380.
- [32] M. Bochicchio, L. Maiani, G. Martinelli, G. C. Rossi, and M. Testa, Nucl. Phys. **B262**, 331 (1985).
- [33] M. Lüscher, S. Sint, R. Sommer, P. Weisz, and U. Wolff, Nucl.Phys. **B491**, 323 (1997), hep-lat/9609035.
- [34] M. Guagnelli et al. (ALPHA Collaboration), Nucl.Phys. **B595**, 44 (2001), hep-lat/0009021.
- [35] M. Della Morte, R. Hoffmann, and R. Sommer, JHEP **0503**, 029 (2005), hep-lat/0503003.
- [36] W. Press, B. Flannery, S. Teukolsky, and W. Vetterling, *Numerical Recipes in C: The Art of Scientific Computing* (Cambridge University Press, 1992), ISBN 0521431085, URL <http://www.amazon.ca/exec/obidos/redirect?tag=citeulike09-20&path=ASIN/0521431085>.
- [37] M. Gell-Mann, R. Oakes, and B. Renner, Phys.Rev. **175**, 2195 (1968).
- [38] P. Gerber and H. Leutwyler, Nucl.Phys. **B321**, 387 (1989).
- [39] M. Asakawa, T. Hatsuda, and Y. Nakahara, Prog. Part. Nucl. Phys. **46**, 459 (2001), hep-lat/0011040.
- [40] Y. Nakahara, M. Asakawa, and T. Hatsuda, Phys. Rev. **D60**, 091503 (1999), hep-lat/9905034.
- [41] T. Yamazaki et al. (CP-PACS Collaboration), Phys.Rev. **D65**, 014501 (2002), hep-lat/0105030.
- [42] H. R. Fiebig, Phys.Rev. **D65**, 094512 (2002), hep-lat/0204004.
- [43] K. Sasaki, S. Sasaki, and T. Hatsuda, Phys.Lett. **B623**, 208 (2005), hep-lat/0504020.
- [44] F. Karsch, E. Laermann, P. Petreczky, S. Stickan, and I. Wetzorke, Phys.Lett. **B530**, 147 (2002), hep-lat/0110208.
- [45] G. Aarts, C. Allton, J. Foley, S. Hands, and S. Kim, Phys. Rev. Lett. **99**, 022002 (2007), hep-lat/0703008.
- [46] G. Aarts, C. Allton, M. B. Oktay, M. Peardon, and J.-I. Skullerud, Phys. Rev. **D76**, 094513 (2007), 0705.2198.
- [47] H.-T. Ding, A. Francis, O. Kaczmarek, F. Karsch, E. Laermann, et al., Phys.Rev. **D83**, 034504 (2011), 1012.4963.
- [48] H. Ding, A. Francis, O. Kaczmarek, F. Karsch, H. Satz, et al., J.Phys. **G38**, 124070 (2011), 1107.0311.
- [49] H. Ding, A. Francis, O. Kaczmarek, F. Karsch, H. Satz, et al., Phys.Rev. **D86**, 014509 (2012), 1204.4945.
- [50] F. Karsch, E. Laermann, P. Petreczky, and S. Stickan, Phys.Rev. **D68**, 014504 (2003), hep-lat/0303017.
- [51] G. Aarts and J. M. Martinez Resco, Nucl. Phys. **B726**, 93 (2005), hep-lat/0507004.
- [52] T. Bhattacharya, M. I. Buchoff, N. H. Christ, H. T. Ding, R. Gupta, et al. (2014), 1402.5175.
- [53] M. Lüscher (1998), hep-lat/9802029.
- [54] K. Chetyrkin, V. Spiridonov, and S. Gorishnii, Phys.Lett. **B160**, 149 (1985).